Twisting, bending, stretching: strategies for making ferromagnetic [Mn^{III}_3] triangles†

Ross Inglis,[a] Stephanie M. Taylor,[a] Leigh F. Jones,[a] Giannis S. Papaefstathiou,[b] Spyros P. Perlepes,[c] Saiti Datta,[d] Stephen Hill,[d] Wolfgang Wernsdorfer[e] and Euan K. Brechin*[a]

Received 17th June 2009, Accepted 14th September 2009
First published as an Advance Article on the web 2nd October 2009
DOI: 10.1039/b911820a

The synthesis and characterisation of a large family of trimetallic [Mn^{III}_3] Single-Molecule Magnets is presented. The complexes reported can be divided into three categories with general formulae (*type 1*) [Mn^{III}_3O(R-sao)$_3$(X)(sol)$_{3-4}$] (where R = H, Me, ^{t}Bu; X = ^-O_2CR (R = H, Me, Ph *etc*); sol = py and/or H_2O), (*type 2*) [Mn^{III}_3O(R-sao)$_3$(X)(sol)$_{3-5}$] (where R = Me, Et, Ph, ^{t}Bu; X = ^-O_2CR (R = H, Me, Ph *etc*); sol = MeOH, EtOH and/or H_2O), and (*type 3*) [Mn^{III}_3O(R-sao)$_3$(sol)$_3$(XO_4)] (where R = H, Et, Ph, naphth; sol = py, MeOH, β-pic, Et-py, ^{t}Bu-py; X = Cl, Re). We show that deliberate structural distortions of the molecule can be used to tune the observed magnetic properties. In the crystals the ferromagnetic triangles are involved in extensive inter-molecular H-bonding which is clearly manifested in the magnetic behaviour, producing exchange-biased SMMs. These interactions can be removed by ligand replacement to give "simpler" SMMs.

Introduction

The synthesis and study of polymetallic clusters containing paramagnetic transition metal ions has provided scientists with molecules displaying fascinating new physics.[1-19] The emergence of *Molecular Nanomagnets* in proposed applications as diverse as information storage, molecular spintronics, quantum computation and magnetic refrigeration has seen synthetic chemists, physicists, theoreticians and materials scientists working in tandem to create, understand and design molecules with specific properties. For example, combining the organic chemistry of rotaxanes with the inorganic chemistry of heterometallic wheels recently resulted in the assembly a beautiful family of inorganic-organic molecular shuttles comprising inorganic rings assembled around organic threads.[20] The amalgamation of two previously unconnected areas of chemistry is a timely illustration that with some imagination chemists can create molecules with untold potential.

Oxide-centred [Mn^{III}_3] triangles have interested inorganic co-ordination chemists for many years not only for the study of their intrinsic magnetism but because they represent the basic building block from which a plethora of beautiful polymetallic clusters with fascinating physical properties are constructed.[21] The first ferromagnetic [Mn^{III}_3O]$^{7+}$ triangle, [Mn_3O(bamen)](ClO_4) (where H_2bamen is 1,2-bis(biacetylmonoximeimino)ethane was only reported in 2002,[22] with a second example, [Mn_3O(mpko)$_3$-(O_2CR)$_3$](ClO_4) (mpkoH = methyl 2-pyridyl ketone oxime) appearing in 2005.[23] Both molecules can be considered simple structural analogues of the well known basic carboxylates of general formula [$Mn^{III}_3O(O_2CR)_6L_3$]$^+$ (R = Me, Et, Ph; L = H_2O, py, MeCN *etc*) in which the bridging carboxylates (Mn-O-C-O-Mn) have been replaced with bridging oximes (Mn-N-O-Mn) - all six in the former and only the "lower" three in the latter (Fig. 1).

The publication of these two molecules was fascinating and prompted us to ask the following questions: why do these oxime-bridged triangles display dominant ferromagnetic exchange between the metal centres and thus $S = 6$ ground states, while the carboxylate-only [Mn^{III}_3O] triangles display dominant antiferromagnetic exchange? And why did our own (and at the time unpublished) oxime-based triangles of general formula [Mn^{III}_3O(sao)$_3$(O_2CR)L_4] (where saoH$_2$ is salicylaldoxime and L = H_2O, py; Fig. 1)[24] display dominant antiferromagnetic exchange and $S = 2$ ground states?

An initial inspection of the molecular structures (Fig. 1) of the three molecules provided a possible clue to the puzzle and implanted an idea. Both [Mn_3O(bamen)](ClO_4) and [Mn_3O(mpko)$_3$(O_2CR)$_3$](ClO_4) (Fig. 1) have structures that are essentially analogous to the well known [$Mn^{III}_3O(O_2CR)_6L_3$]$^+$ family[25] where the bridging oximes simply replace the carboxylates and thus occupy a plane at approximately 60° to the [Mn_3O] plane, while the oxime bridges in the [Mn^{III}_3O(sao)$_3$(O_2CR)L_4] family are in exactly the same plane as the [Mn_3O] unit (Fig. 1). Clearly these three family types, despite being closely related, are different because their formulae and structural architectures are not the same, nevertheless we wondered if forcing or "twisting" the planar equatorial Mn-N-O-Mn unit out of the [Mn^{III}_3O] plane in the latter (R-saoH$_2$) family would have any significant effect and if so whether this would be large enough to switch the pairwise exchange from antiferromagnetic to ferromagnetic.

[a]*School of Chemistry, The University of Edinburgh, West Mains Road, Edinburgh, UK EH9 3JJ. E-mail: ebrechin@staffmail.ed.ac.uk; Fax: +44 11–275–4598; Tel: +44 131 650 7545*
[b]*Laboratory of Inorganic Chemistry, Department of Chemistry, National and Kapodistrian University of Athens, Panepistimiopolis, 157 71, Zografou, Greece*
[c]*Department of Chemistry, University of Patras, 26504, Patras, Greece*
[d]*National High Magnetic Field Laboratory and Florida State University, Tallahassee, FL32310, USA*
[e]*Institut Néel, CNRS & Université J. Fourier, BP 166, 38042, Grenoble, France*

† Electronic supplementary information (ESI) available: Fig. SI1–SI3. CCDC reference numbers 736436–736445. For ESI and crystallographic data in CIF or other electronic format see DOI: 10.1039/b911820a

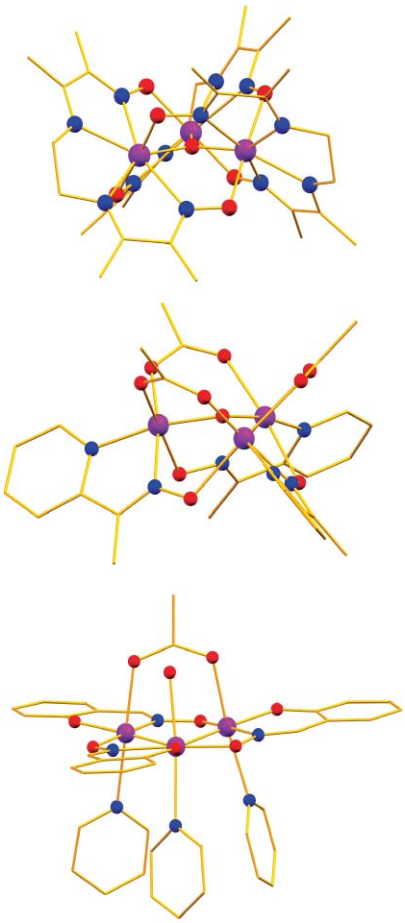

Fig. 1 Top-bottom: the molecular structures of $[Mn_3O(bamen)]^+$, $[Mn_3O(mpko)_3(O_2CR)_3]^+$ and $[Mn^{III}{}_3O(sao)_3(O_2CR)L_4]$ (R = Me; L = py, H_2O). Colour code: Mn = purple, O = red, N = blue, C = gold.

We speculated that a change from salicylaldoxime to its alkyl/aryl-substituted derivatives (R-saoH_2, Scheme 1) would provide the steric perturbation required to do this, and indeed this has already proven successful for a family of hexametallic single-molecule magnets (SMMs) of formula $[Mn_6O_2(R\text{-}sao)_6(X)_2(L)_{4\text{-}6}]$ (R = H, Me, Et, Ph; X = O_2CR', halide; L = EtOH, MeOH, H_2O) with spin ground states ranging from $S = 4$ to $S = 12$.[26] Herein we return to the $[Mn^{III}{}_3O(sao)_3(O_2CR)L_4]$ molecules and report a family of over twenty $[Mn^{III}{}_3]$ triangles whose ground state spin values appear to be controlled by the puckering or twisting of their central cores. Initial studies by us,[27] and more recently by others on related systems[28] have suggested this to be the case.

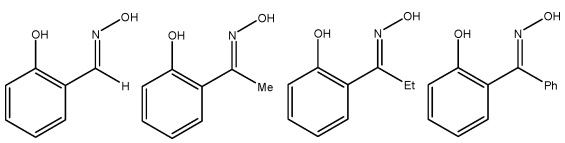

Scheme 1 The R-saoH_2 family of pro-ligands. saoH_2, R = H; Me-saoH_2, R = Me; Et-saoH_2, R = Et; Ph-saoH_2, R = Ph.

The puckering of a planar $[Mn_3O(oxime)_3]$ triangle can be achieved in three ways: (a) through the use of derivatized salicylaldoxime (R-saoH_2) ligands that occupy the equatorial ($[Mn_3]$) plane - in the same manner as that already achieved for the $[Mn_6]$ SMMs; (b) by employing small "pincer" type tripodal ligands (ClO_4^-, ReO_4^- *etc*) to sit on the "upper" triangular face; and (c) by employing large sterically bulky ligands to occupy the "lower" triangular face.[27]

Results and discussion

The twenty-one complexes (Table 1) can be divided into three structural types. Complexes **3-6** and **8-10** can be represented by the general formula (*type 1*) $[Mn^{III}{}_3O(R\text{-}sao)_3(X)(sol)_{3\text{-}4}]$ (where R = H, Me, ^{t}Bu; X = ^-O_2CR (R = H, Me, Ph *etc*); sol = py and/or H_2O). Complexes **7**, **11-12**, **14-15** and **20** can be described by (*type 2*) $[Mn^{III}{}_3O(R\text{-}sao)_3(X)(sol)_{3\text{-}5}]$ (where R = Me, Et, Ph, ^{t}Bu; X = ^-O_2CR (R = H, Me, Ph *etc*); sol = MeOH, EtOH and/or H_2O), and complexes **1-2**, **13**, **16-19** and **21** can be represented by the formula (*type 3*) $[Mn^{III}{}_3O(R\text{-}sao)_3(sol)_3(XO_4)]$ (where R = H, Et, Ph, naphth; sol = py, MeOH, β-pic, Et-py, ^{t}Bu-py; X = Cl, Re) (Fig. 2). Interatomic distances and angles relevant to the discussion herein are shown in Table 1. Each complex consists of the same core comprising a $[Mn^{III}{}_3O]^{7+}$ triangular unit (Fig. 2) with three R-sao^{2-} ligands bridging between adjacent Mn^{III} centres in a $\eta^1{:}\eta^1{:}\eta^1{:}\mu$-fashion. For *type 1* complexes the three axial sites at the base of the molecule are occupied by pyridine molecules. The $\eta^1{:}\eta^1{:}\mu$-bridging carboxylate ligand connects two Mn^{III} centres (Mn1 and Mn2) on the upper face of the molecule. The remaining site on the upper face is occupied by a pyridine or H_2O molecule in **3**, **6** and **9**, but remains unoccupied in **4**, **5**, **8** and **10** (Mn3 is five-coordinate) owing to the presence of a bulkier carboxylate group. Each Mn^{III} centre adopts a distorted octahedral geometry and displays Jahn–Teller elongation, with Mn-O_2CR bond lengths in the range 2.13-2.27 Å and Mn-N bond lengths in the range 2.22-2.58 Å; *i.e.* the JT axes are perpendicular to the $[Mn_3]$ plane. In **8**, a six-coordinate Na^+ ion connects two symmetry-equivalent $\{Mn^{III}{}_3O(Me\text{-}sao)_3(O_2C_{15}H_9)(py)_3\}$ moieties together forming a $[\{Mn_3\}\text{-}Na\text{-}\{Mn_3\}]$ dimer, with charge balanced by two symmetry-equivalent ClO_4^- counter ions and one pyridinium cation, which is H-bonded to the pyridine solvent molecule. *Type 2* molecules have the same core structure as *type 1*, the only difference being the terminally bonded pyridine molecules are replaced by alcohol and/or H_2O molecules. Complexes **7** and **11** have the carboxylate bonded terminally with the vacant site on the other Mn centre taken up by another solvent molecule. In **11** the Mn centre attached to the carboxylate is five-coordinate. Complex **14** has two carboxylate ligands in its structure, with one bridging Mn1 and Mn2 on the upper face and the other terminally bound to Mn3 on the lower face. The charge is balanced by a protonated triethanolamine ligand which is connected to Mn3.

Type 3 molecules have the upper face of the molecule capped by a $\eta^1{:}\eta^1{:}\eta^1{:}\mu_3$ coordinated XO_4^- (X = Cl, Re) anion with the three axial sites on the lower face occupied by solvent molecules.

Type 2 molecules (and complex **13**) have extensive inter-molecular interactions propagated by the terminal alcohol/H_2O molecules and carboxylate ligands in all three dimensions that severely affect their magnetic behaviour (*vide infra*). For example, the molecules in **12** are arranged with their upper faces face-to-face. The water molecule which is attached on the upper face of the Mn_3 triangle is hydrogen bonded to a carboxylate O-atom [∠O2-H22···O24 160.0°, O···O 2.913(2) Å and H···O 2.130 Å] that belongs to the same cluster and to a phenolate

Table 1 Selected interatomic distances (Å) and angles (°) for complexes **1-21**

Complex	Mn-(μ_3-O) distance (Å) Mn1-O, Mn2-O, Mn3-O	Mn-(μ_3-O)-Mn angles (°) Mn1-2, Mn2-3, Mn1-3	Mn_3 plane-μ_3O distance (Å)	Mn-O_2CR/Mn-O_4Cl distance (Å)
$[Mn_3O(naphth\text{-}sao)_3(py)_3(ClO_4)]$ (**1**)	1.8898(25)	118.327(132)	0.2464(0.0025)	2.4901(33)
$[Mn_3O(sao)_3(Et\text{-}py)_3(ClO_4)]$(**2**)	1.8981(9)	117.64(6)	0.2944(0.0042)	2.463(3)
$[Mn_3O(sao)_3(O_2CPh)(H_2O)(py)_3]$ (**3**)	1.9021(5), 1.9021(6), 1.9014(7)	116.97(5)	0.3350(0.0023)	n.a.
$[Mn_3O(sao)_3(O_2C\text{-}naphth)(py)_3]\cdot py$ (**4**)	1.9126(56), 1.9343(49), 1.8843(53)	112.271(291), 113.197(271), 117.666(272)	0.4602(0.0055)	2.1967(72), 2.2031(72)
$[Mn_3O(sao)_3(O_2CPh(Me_4))(py)_3]\cdot EtOH$ (**5**)[a]	1.9112(32), 1.9081(33), 1.8740(42)	112.80(2), 116.30(2), 119.00(2)	0.3834(0.0043)	2.1656(38), 2.1870(43)
	1.9177(41), 1.8700(33), 1.9080(32)	112.70(2), 118.20(2), 117.10(2)	0.3548(0.0035)	2.1674(37), 2.1870(45)
$[Mn_3O(sao)_3(O_2CCH_3)(H_2O)(py)_3]\cdot py$ (**6**)	1.8972(10), 1.8979(8), 1.8980(9)	116.59(7), 116.55(7), 116.63(7)	0.0800(0.0034)	2.241(11)
$[Mn_3O(Me\text{-}sao)_3(O_2CCH_3)(MeOH)_5]\cdot Me\text{-}saoH_2$ (**7**)	1.855(3), 1.881(3), 1.893(3)	119.88(15), 119.01(15), 120.57(15),	0.4654(0.0029)	2.457(4)
$(Na)(PyH)[Mn_3O(Me\text{-}sao)_3(O_2C\text{-}anthra)(py)_3]_2[ClO_4]_2\cdot py$ (**8**)	1.9195(23), 1.9032(18), 1.8789(21)	110.80(1), 114.86(1), 116.99(1)	0.3590(0.0010)	2.1924(24), 2.2655(27)
$[Mn_3O(Me\text{-}sao)_3(O_2CCH_3)(py)_4]\cdot 2py$ (**9**)	1.8799(10), 1.8988(10), 1.9005(10)	113.57(5), 117.89(5), 118.00(5)	0.2825(0.0027)	2.1519(11), 2.1616(11)
$[Mn_3O(tBu\text{-}sao)_3(O_2CPh(OMe)_3))(py)_3]$ (**10**)	1.8670(27), 1.9013(24), 1.8968(30)	114.696(14), 118.778(14), 119.925(16)	0.0022(0.0027)	2.1262(34), 2.2078(36)
$[Mn_3O(tBu\text{-}sao)_3(O_2CPh(CH_3)_2)(MeOH)_4]$ (**11**)	1.8967(31), 1.8910(23), 1.8862(30)	119.232(15), 120.618(14), 120.15(14)	0.2648(0.0015)	2.0777(28)
$O(Et\text{-}sao)_3(O_2CPh(Cl)_2)(H_2O)(MeOH)_3]$(**12**)	1.8792(14), 1.8884(13), 1.8738(14)	115.33(7), 120.10(7), 118.71(7)	0.1792(0.0017)	2.2036(15), 2.2082(15)
$[Mn_3[Mn_3O(Et\text{-}sao)_3(MeOH)_3(ClO_4)]$ (**13**)	1.8770(2), 1.8791(2), 1.8794(3)	119.150(1), 119.022(7), 119.130(8)	0.2314(0.0022)	2.5496(11)
$[Mn_3O(Et\text{-}sao)_3(O_2CPh)_2(teaH_4)(H_2O)_2]$ (**14**)	1.8794(19), 1.871(2), 1.8762(19),	115.18(10), 120.59(10), 119.72(11),	0.2274(0.0026)	2.180(2), 2.288(2), 2.189(2)
$[Mn_3O(Et\text{-}sao)_3(O_2CPh(CF_3)_2)(EtOH)(H_2O)_3]\cdot EtOH$ (**15**)	1.8803(26), 1.8674(28), 1.8740(26)	115.83(13), 119.96(14), 119.84(14)	0.2776(0.0026)	2.1779(36), 2.3222(28)
$[Mn_3O(Et\text{-}sao)_3(\beta\text{-}pic)_3(ClO_4)]$ (**16**)	1.9007(4), 1.8995(4), 1.9005(4)	117.917(1), 117.865(1), 117.927(1)	0.2754(0.0025)	2.5667(18)
$[Mn_3O(Et\text{-}sao)_3(Et\text{-}py)_3(ClO_4)]$ (**17**)	1.8936(4), 1.8934(4), 1.8947(4)	117.909(1), 117.961(1), 117.900(1)	0.2664(0.0045)	2.5416(15)
$[Mn_3O(Et\text{-}sao)_3(tBu\text{-}py)_3(ClO_4)]$ (**18**)[a]	1.8866(11), 1.8883(9), 1.8883(10)	118.070(31), 117.986(30), 118.07(3)	0.2916(0.0040)	2.4871(34), 2.4871(33)
	1.9008(8), 1.9008(9), 1.9008(10)	117.690(22), 117.690(24), 117.690(28)	0.0371(0.0027)	2.4703(29), 2.4703(30)
$[Mn_3O(Et\text{-}sao)_3(EtOH)(H_2O)_2(ReO_4)]\cdot 3EtOH$ (**19**)	1.892(3), 1.888(3), 1.881(3)	121.33(17), 119.69(17), 118.86(16)	0.1778(0.0015)	2.382(4), 2.377(3), 2.443(4)
$[Mn_3O(Ph\text{-}sao)_3(O_2C\text{-}anthra)(MeOH)_4]\cdot(Ph\text{-}saoH_2)$ (**20**)	1.8744(14), 1.8710(17), 1.8696(16)	115.80(8), 121.54(8), 119.98(8)	0.1778(0.0015)	2.1665(22), 2.2059(19)
$[Mn_3O(Ph\text{-}sao)_3(\beta\text{-}pic)_3(ClO_4)]$ (**21**)	1.8820(18), 1.9044(18), 1.8963(17)	117.428(92), 118.214(92), 118.946(93)	0.2565(0.0019)	2.6553(25), 2.5378(22), 2.4829(22)

[a] Two Mn_3 complexes in the asymmetric unit, therefore two sets of data documented. $teaH_3$ = triethanolamine.

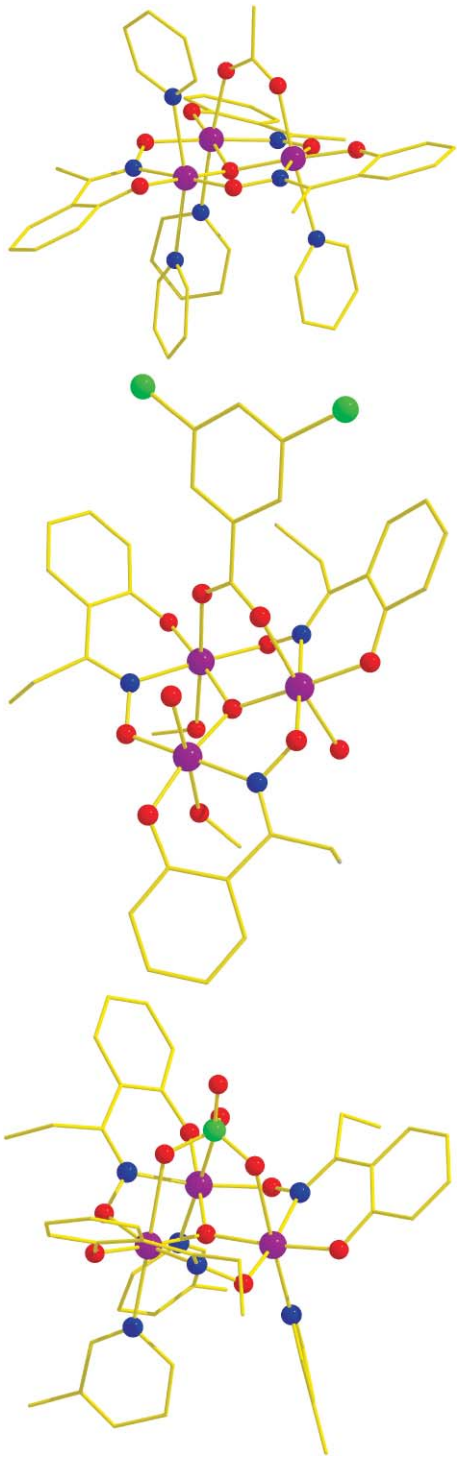

Fig. 2 The molecular structures of **9** (top, *type 1*), **12** (middle, *type 2*) and **16** (bottom, *type 3*) representing the three different structural types in the [Mn_3] family. Colour code: Mn = purple, O = red, N = blue, C = gold, Cl = green.

O-atom of a neighbouring cluster [∠O2-H21 · · · O13 (1 − x, −y, −z) 174.0°, O · · · O 2.791(2) Å and H · · · O 1.980 Å] creating a hydrogen-bonded dimer (Fig. SI1†). The dimers assemble with the bases of the Mn_3 triangles face-to-face through two complementary hydrogen bonds that involve a methanolic OH group of one cluster and a phenolate O- atom of a neighboring cluster [∠O25-H251 · · · O11 (1 − x, −y, 1 − z) 165.0°, O · · · O 2.783(2) Å and H · · · O 1.980 Å] to create a zig-zag chain that runs parallel to the *a* axis (Fig. SI1†). All Mn_3 mean planes within a chain are parallel, with the inter-plane distances being 4.011 Å within a dimer and 3.471 Å between dimers, respectively. Clusters of **15** assemble through the coordinated water molecules of the upper face of the Mn_3 triangle and a phenolate O-atom to form a hydrogen-bonded dimer [∠O47-H472 · · · O26 (1 − x, −y, 2 − z) 156.0°, O · · · O 2.812(4) Å and H · · · O 2.060 Å]. The dimers assemble *via* the coordinated water and ethanol molecules of the Mn_3 triangle base with the lattice ethanol and water molecules to form a two-dimensional hydrogen-bonded layer that runs parallel to the *ab* plane (Fig. SI2†). All Mn_3 mean planes within a layer are again parallel and form an angle of approximately 42° with respect to the mean plane of the layer and the *ab* plane. The inter-plane $Mn_3 \cdots Mn_3$ distance within a dimer is 3.929 Å.

The presence of the capping ClO_4^- anion on the upper triangular face of **13** and the absence of solvate molecules forces the Mn_3 clusters to self-assemble through the three MeOH molecules which are attached on the base of the triangle. Each Mn_3 is hydrogen-bonded to three neighbours through six complementary hydrogen bonds (one unique) that involve the terminal MeOH molecules and the phenolate O atoms of the Et-sao^{2-} ligands [∠O15-H1 · · · O8 (1 − x, 1 − y, 1 − z) 168°, O · · · O 2.734(1) Å and H · · · O 1.95 Å]. In this arrangement an undulated two-dimensional hydrogen bonded layer forms that conforms to a (6,3) net and lies parallel to the *ab* plane (Fig. 3). The Mn_3 triangles are arranged with their upper faces above and below the plane of the hydrogen-bonded framework with their mean planes parallel to each other and to the mean plane of the framework. The layers stack in an off-set fashion with the Mn_3 triangles of one layer lying above and below the hexagonal cavities of the two neighbouring frameworks. The Mn_3 clusters in **20** have assembled with a Ph-saoH_2 molecule of crystallisation. The MeOH molecule at the upper face of the Mn_3 triangle forms an intra-molecular hydrogen bond with one carboxylate O-atom [∠O18-H18 · · · O24 162°, O · · · O 2.876(3) Å and H · · · O 2.09 Å]. Two of the three MeOH molecules at the base of the triangle are hydrogen-bonded with themselves [∠O17-H17 · · · O15 167°, O · · · O 2.833(3) Å and H · · · O 2.02 Å and ∠O15-H15 · · · O16 171°, O · · · O 2.695(2) Å and H · · · O 1.90 Å] with the third being attached to the Ph-saoH_2 molecule [∠O16-H16 · · · N99 163°, O · · · O 2.751(3) Å and H · · · O 1.95 Å]. The salicyl OH group of the Ph-saoH_2 molecule forms an intra-molecular hydrogen bond with the oximic O-atom [∠O19-H19 · · · O109 168°, O · · · O 2.577(3) Å and H · · · O 1.69 Å] while the latter attaches to a phenolate O-atom of the triangle [∠O109-H109 · · · O103 163°, O · · · O 2.643(2) Å and H · · · O 1.82 Å]. The Mn_3·Ph-saoH_2 units interact with five neighbouring assemblies through ten (five unique) C-H · · · π interactions to create a three-dimensional framework with $4^6.6^4$-**bnn** topology (Fig. 3).[29]

Magnetic studies

Dc magnetic susceptibility studies were carried out on powdered crystalline samples of **1-21** in the 5-300 K temperature range in a field of 0.1 T. The magnetic susceptibility data obtained for each were simulated using the program MAGPACK[30] employing the Hamiltonians in equations (1)-(3) (Scheme 2) to provide the isotropic parameters summarised in Table 2. No attempt was made

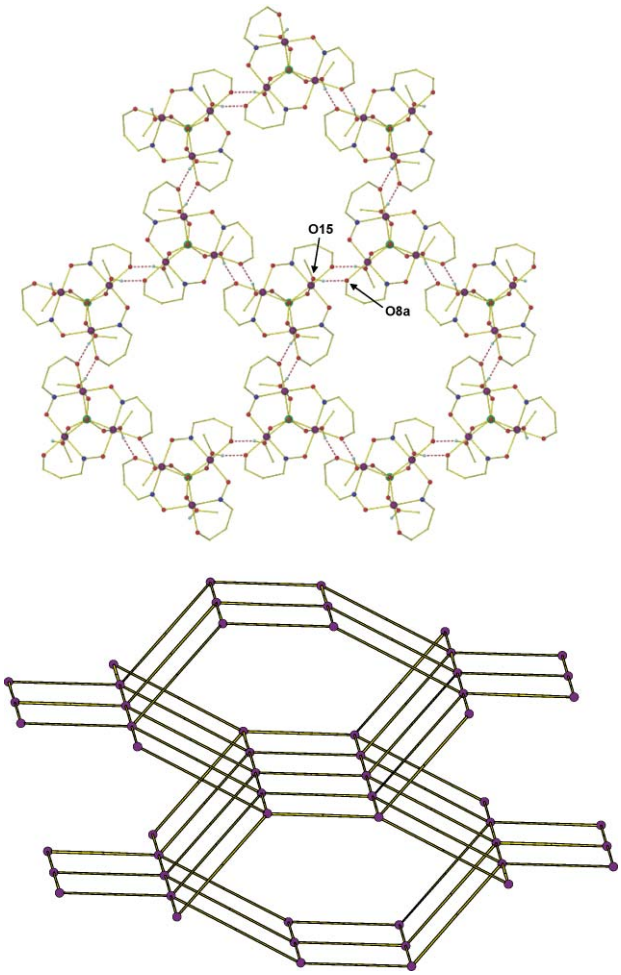

Fig. 3 (top) The hydrogen bonded (6,3) layer in **13**. Most hydrogen and carbon atoms have been omitted for clarity. Symmetry code: a 1 − x, 1 − y, 1 − z. (bottom) The $4^6.6^4$-**bnn** hydrogen bonded network found in **20**. Purple spheres represent the Mn_3·Ph-saoH_2 assemblies while the gold lines represent the C-H $\cdots$ π interactions.

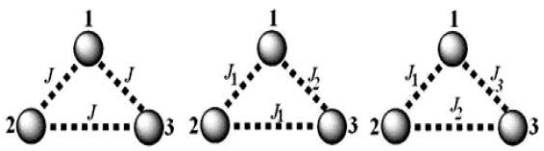

Scheme 2 Schematic detailing the *1*, *2* and *3*-*J* models employed to simulate the experimental data for **1-21**.

to simulate the data for **5** and **18** as the crystal structures contain two independent molecules with different geometries (Table 1), and for **3** and **6** as the crystal structures are highly disordered. We also stress that what follows should be regarded as a qualitative interpretation. It is clear that these molecules (and their [Mn_6] forefathers) are complicated molecules in which excited states (a direct result of the weak magnetic coupling) and inter-molecular interactions play an important role. The analysis is thus confined within our simplistic model, but allows us to identify and define clear trends in behaviour which is invaluable for future synthetic molecular design. More detailed studies on individual family members will be presented in future papers.

$$\hat{H} = -2J\,(\hat{S}_1\hat{S}_2 + \hat{S}_2\hat{S}_3 + \hat{S}_1\hat{S}_3) \quad (1)$$

$$\hat{H} = -2J_1\,(\hat{S}_1\hat{S}_2 + \hat{S}_2\hat{S}_3) - 2J_2\,(\hat{S}_1\hat{S}_3) \quad (2)$$

$$\hat{H} = -2J_1\,(\hat{S}_1\hat{S}_2) - 2J_2\,(\hat{S}_2\hat{S}_3) - 2J_3\,(\hat{S}_1\hat{S}_3) \quad (3)$$

The $\chi_M T$ *vs.* T data are plotted in Fig. 4 along with their associated simulations (solid lines). Room-temperature $\chi_M T$ values for **1-11** range from 7.25 to 8.69 cm^3 K mol^{-1}. This is lower than the expected spin-only ($g = 2$) value for three non-interacting Mn^{III}

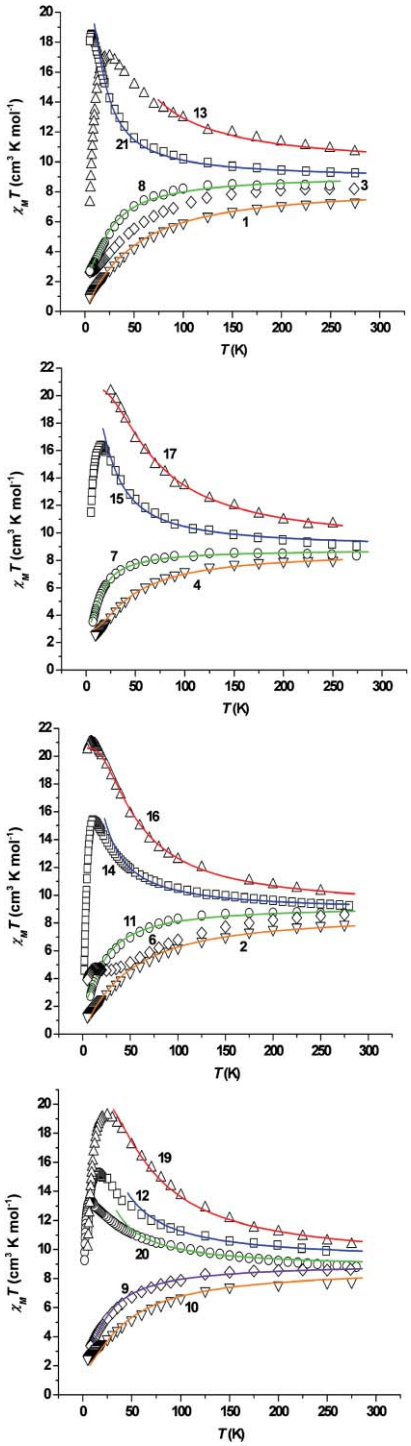

Fig. 4 Plots of $\chi_M T$ *vs.* T for complexes **1-21**. The solid lines represent simulations of the experimental data. For parameters see Table 2.

Table 2 Magnetostructural parameters for complexes **1-21**; Mn-N-O-Mn torsion angles (α) *vs.* *J* and *S*

Complex	Crystal System	Space Group	α/° Mn1-2/ Mn2-3/Mn1-3	JT tilt/° Mn1/ Mn2/Mn3	J/cm^{-1}[a] $J_1/J_2/J_3$	S[b]	1st exc. st. (cm^{-1})[b]	g[c]	D/cm^{-1}[d]	τ_0/s[e]	U_{eff}/K[e]	θ/K[a]
(**1**)	Cubic	Pa-3	4.11	5.29	–3.10	0	1(6.2)	1.94	n.a.	n.a.	n.a.	–36.00
(**2**)	Trigonal	P-3	13.11	1.43	–3.02	0	1(6.04)	1.98	n.a.	n.a.	n.a.	–43.73
(**3**)	Trigonal	P-3	8.96	8.45	n.a.	2	n.a.	1.96	–2.39	n.a.	n.a.	–28.75
(**4**)	Triclinic	P-1	27.88, 35.82, 6.64	11.19, 2.53	–2.95, +0.16	2	1(13.08)	1.98	–2.33	n.a.	n.a.	–21.44
(**5**)	Triclinic	P-1	31.99, 11.06, 3.04 24.38, 5.33, 11.06	2.64, 11.74 6.62, 16.24	n.a.	n.a.	n.a.	n.a.	n.a.	n.a.	n.a.	n.a.
(**6**)	Trigonal	P-3	7.32	10.16	n.a.	2	n.a.	n.a.	n.a.	n.a.	n.a.	–44.52
(**7**)	Monoclinic	P21	26.78, 30.70, 38.11	4.51, 7.35, 1.30	–1.20, –0.96, +0.56	2	3(6.46)	1.98	n.a.	n.a.	n.a.	0.545
(**8**)	Triclinic	P-1	16.35, 11.74, 26.58	4.68, 15.75	–1.20, –1.94, –0.40	2	1(2.89)	2.02	–3.61	n.a.	n.a.	–2.96
(**9**)	Monoclinic	$P2_1/n$	4.15, 4.45, 23.44	10.06, 14.72, 5.73	–1.56, –0.36	2	1(3.36)	2.01	n.a.	n.a.	n.a.	–12.46
(**10**)	Monoclinic	C2/c	14.38, 35.36, 1.31	12.80, 17.95, 6.92	–3.85, –3.05, +0.4	2	1(16.93)	1.98	–3.77	n.a.	n.a.	–20.51
(**11**)	Triclinic	P-1	13.07, 20.23, 32.09	2.34, 6.89	–1.65, +0.10	2	1(7.40)	2.02	n.a.	n.a.	n.a.	–1.32
(**12**)	Triclinic	P-1	44.60, 38.17, 39.07	11.37, 7.95, 5.84	+1.84	6	5(22.08)	2.02	–0.59	1.27×10^{-9}	43.69	27.82
(**13**)	Trigonal	R-3	42.12	5.93	+2.80	6	5(33.60)	2.06	–0.77	1.98×10^{-9}	57.02	30.77
(**14**)	Triclinic	P-1	44.60, 35.76, 37.18,	3.97, 16.29, 4.19	+1.40	6	5(16.80)	1.98	–0.92	8.40×10^{-9}	25.73	19.82
(**15**)	Triclinic	P-1	46.66, 38.56, 40.35	6.71, 1.73, 9.00	+1.52	6	5(18.24)	1.98	–0.82	7.40×10^{-9}	42.53	16.98
(**16**)	Trigonal	P-3 c1	44.96	2.78	+3.40	6	5(40.80)	1.99	–0.52	2.97×10^{-8}	42.74	37.47
(**17**)	Trigonal	R-3	46.78	10.20	+4.10	6	5(49.20)	1.98	–0.48	1.46×10^{-8}	47.97	38.19
(**18**)	Trigonal	R 3 c	45.40 40.42	10.35 2.11	n.a.	n.a.	n.a.	n.a.	n.a.	n.a.	n.a.	n.a.
(**19**)	Triclinic	P-1	41.65, 40.25, 43.53	3.68, 1.98, 8.91	+4.02	6	5(48.24)	2.00	–0.75	5.55×10^{-9}	48.31	40.78
(**20**)	Triclinic	P-1	32.98, 34.41, 41.44	3.27, 12.53, 5.25	+0.85, +1.44	6	5(13.80)	1.98	–0.51	n.a.	n.a.	20.44
(**21**)	Monoclinic	$P2_1/n$	46.22, 39.31, 40.78	4.49, 7.58, 12.07	+1.20	6	5 (14.40)	1.98	–0.37	n.a.	n.a.	15.51

[a] Calculated from dc susceptibility studies. [b] Calculated from both dc susceptibility and magnetization measurements. The latter were collected in the field and temperature ranges 0–7 T and 2–7 K. In each case the data were fit by a matrix-diagonalization method to a model that assumes only the ground state is populated, includes axial zero-field splitting ($D\hat{S}_z^2$), and carries out a full powder average. The corresponding Hamiltonian is $\hat{H} = D(\hat{S}_z^2 - S(S+1)/3) + \mu_B g H \hat{S}$ where D is the axial anisotropy, μ_B is the Bohr magneton, $\hat{S}_z$ is the easy-axis spin operator, and H is the applied field (see ref. 15). [c] Calculated from dc susceptibility measurements. [d] Calculated from magnetization measurements. [e] Calculated from dc susceptibility data and/or single-crystal relaxation measurements performed on a micro-SQUID; n.a. = not available.

centres of 9 cm^3 K mol^{-1}, suggesting the presence of dominant antiferromagnetic exchange between the Mn^{III} centres. The $\chi_M T$ values then decrease gradually until approximately 100 K where they decrease more rapidly to values between 0.93 and 3.92 cm^3 K mol^{-1} at 5 K. For all complexes the data was simulated using the simplest model possible. Thus, the data for complexes **1-2** was simulated using the *1-J* model of equation (1) and Scheme 2, giving the parameters $S = 0$, $g = 1.94$, $J = -3.10$ cm^{-1} and $S = 0$, $g = 1.98$, $J = -3.02$ cm^{-1}, with the first excited state ($S = 1$) 6.20 cm^{-1} and 6.04 cm^{-1} above the ground state, respectively. The data obtained for complexes **4**, **9** and **11** were simulated using the *2-J* model of equation (2), with J_1 mediated through oxide, oxime and carboxylate, and with $J_2 = J_3$ mediated through oxide and oxime only. Despite many attempts using the *2-J* model, the data for complexes **7**, **8** and **10** could only be simulated using the *3-J* model of equation (3) and Scheme 2 in which $J_1 \neq J_2 \neq J_3$. These results are all summarised in Table 2.

For **12-15**, **19** and **20** the room temperature $\chi_M T$ values range from 9.06 to 10.67 cm^3 K mol^{-1}, indicating the presence of ferromagnetic exchange between the Mn^{III} centres. In each case the $\chi_M T$ values increase gradually as temperature is decreased before increasing more rapidly at lower temperatures, reaching maximum values of between ~13 and ~19 cm^3 K mol^{-1}. A sharp drop in $\chi_M T$ then occurs for each at ~20 K with the low temperature maxima being significantly smaller than the expected value of 21 cm^3 K mol^{-1} expected for $S = 6$. The drop in $\chi_M T$ is attributed to the strong inter-molecular interactions discussed above (and/or zero-field splitting effects). The ("high temperature") data for **12-15** and **19** was simulated (Fig. 4) using the *1-J* model of equation (1) and afforded the parameters $S = 6$, with J values ranging from 1.40 to 4.02 cm^{-1} (Table 2). This model was unsuccessful for **20** and required the *2-J* model of equation (2), giving $S = 6$, $g = 1.98$, $J_1 = 0.85$ and $J_2 = 1.44$ cm^{-1}. The room temperature $\chi_M T$ values for **16**, **17** and **21** range from ~9.3 to ~10.7 cm^3 K mol^{-1} and increase gradually as temperature is decreased, reaching maximum values of between ~18 and ~21 cm^3 K mol^{-1} at the lowest temperature measured. In each case the data could be simulated with the simple *1-J* model affording $S = 6$, $g = 1.98$, $J = 3.40$ cm^{-1}; $S = 6$, $g = 1.98$, $J = 4.10$ cm^{-1} and $S = 6$, $g = 1.98$, $J = 1.20$ cm^{-1}, respectively. It is clear from Fig. 4 that inter-molecular interactions are playing a very important role in the observed behaviour for all the ferromagnetically coupled complexes. Thus we add a note

of caution to the absolute validity/accuracy of the simulation parameters, though they are well within the range observed for *all* previously reported (and analogous) salicyaldoxime-bridged [Mn(III)$_3$]and [Mn(III)$_6$] clusters.[26,27]

Variable field and temperature dc magnetisation data were collected in the 0.5–7 T and 2–7 K field and temperature ranges. In each case we attempted to fit the data with an axial ZFS plus Zeeman Hamiltonian (4) in the whole field and temperature range,[31]

$$\hat{H} = D(\hat{S}_z^2 - S(S+1)/3) + \mu_B g H \hat{S} \quad (4)$$

where D is the axial zero field splitting parameter, μ_B is the Bohr magneton, $\hat{S}$ is the easy-axis spin operator, and H is the applied field. The results are summarised in Table 2 with representative plots given in Fig. 5. Complexes **3-11** possess a spin ground state $S = 2$ with D values ranging from –2.33 to –3.77 cm^{-1}, while complexes **12-20** have the maximum ground state $S = 6$ with smaller D values ranging from –0.37 to –0.92 cm^{-1}. Despite the ferromagnetically coupled complexes being rather similar in structure, the calculated D values span a wide range, and therefore must be treated with caution. Though one would expect some variation due to the varying Jahn–Teller tilts, it is clear that the strong inter-molecular interactions, disorder (in **15**, **16**, **17**) which causes a distribution in molecular environments, the presence of

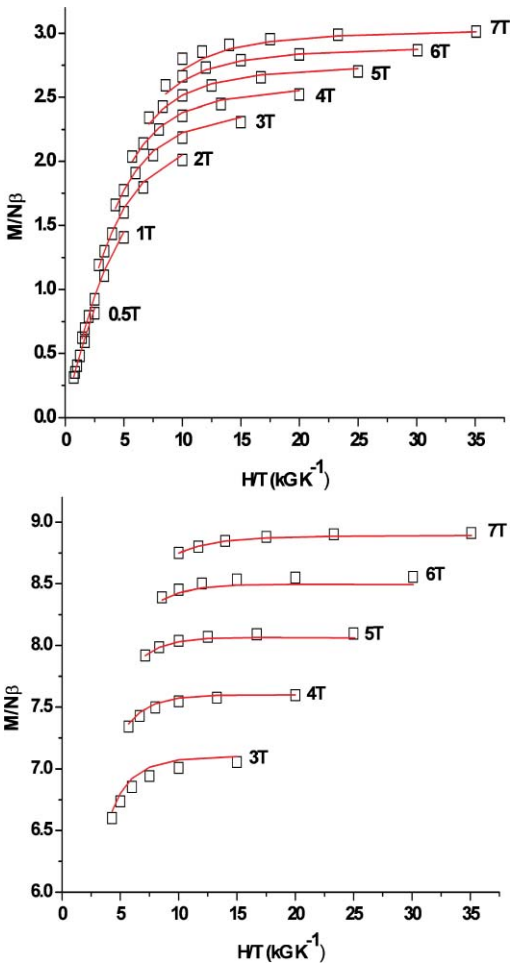

Fig. 5 Plots of reduced magnetisation ($M/N\mu_B$) *versus* H/T for **10** (top) and **15** (bottom) in the noted field ranges and the 2–7 K temperature range. The solid lines correspond to the fit of the data as documented in Table 2.

weak exchange and thus the likely population of excited states in the temperature range studied, and the simplistic model employed, do not allow for an accurate determination of D. Indeed, magnetisation and HF-EPR studies of analogous molecules in which there are no inter-molecular interactions suggest $|D|$ values ≥ 0.8 cm^{-1} which would be consistent only with **14** and **15**.[28] Further proof for this assumption emerges in the analysis of the ac data and single crystal hysteresis loop measurements discussed below.

Ac magnetic susceptibility measurements were carried out on crystalline samples of **3-21** in the 2–10 K temperature range in a 3.5 G ac field oscillating at frequencies ranging from 50 to 1000 Hz. Fully visible out-of-phase (χ_M'') signals indicative of SMM behaviour (Fig. 6 shows those obtained for complex **17**) were observed for *all* $S = 6$ family members except for [Mn_3O(Ph-sao)$_3$(O_2C-anthra)(MeOH)$_4$](Ph-saoH$_2$) (**20**) and [Mn_3O(Ph-sao)$_3$(β-pic)$_3$](ClO_4) (**21**), in which only the tails of the signals were observed. The ac data obtained were combined with single-crystal dc relaxation measurements performed on a μ-SQUID[32] (*vide infra*) and fitted to the Arrhenius equation $\tau = \tau_o \exp(U_{eff}/kT)$, where τ_o is the pre-exponential factor, τ is the relaxation time, U_{eff} is the barrier to the relaxation of the magnetisation and k is the Boltzmann constant, to give the effective barrier to magnetisation reorientation (U_{eff}) for each [Mn_3] complex. These data are summarised in Fig. 6 and Table 2 and span barrier heights of between ~25–57 K. These are amongst the largest effective barriers observed for any low nuclearity SMMs, but they are also *larger* than the theoretical upper limit [$U = S^2|D|$] calculated using the D values obtained from the powder dc magnetisation measurements (~30 K (**12**); ~40 K (**13**); ~48 K (**14**); ~42 K (**15**); ~27 K (**16**); ~25 K (**17**); ~39 K (**19**)). Indeed, only **14** has an effective barrier lower than the theoretical upper limit, with **15** having an experimental value close to its theoretical value. This is to be expected for exchange-coupled SMMs since the spin reversal is hindered by the relatively weak inter-molecular coupling. For stronger inter-molecular exchange coupling one would move away from the biased-SMM regime into a 3D system where the collective modes (domain wall propagation *etc*) would reduce the effective barriers. It also points to a possible underestimation in the zfs parameters obtained from the powder dc measurements, which is confirmed in the single crystal low temperature magnetisation studies (below).

Single crystal hysteresis loop and relaxation measurements

Hysteresis loop and relaxation measurements were carried out on single crystals of all the ferromagnetically coupled complexes using a micro-SQUID assembly, with the field applied along the easy axis of magnetisation.[32] In each case temperature and sweep rate dependent hysteresis loops were observed, confirming SMM behaviour for all complexes. Representative examples are shown for complexes **13** and **16** in Fig. 7. For all *type 2* molecules, in which significant inter-molecular interactions are observed in the crystal lattice, the loops display step-like features separated by plateaus. After saturating the magnetisation, the first resonance is seen in negative fields, indicative of the presence of small and antiferromagnetic inter-molecular interactions as was first observed in the complex [$Mn_4O_3Cl_4$(O_2CEt)$_3$(py)$_3$] which crystallises as a supramolecular H-bonded dimer of cubanes ([Mn_4]$_2$).[33] The hysteresis loops show that the collective spins of each [Mn_3]

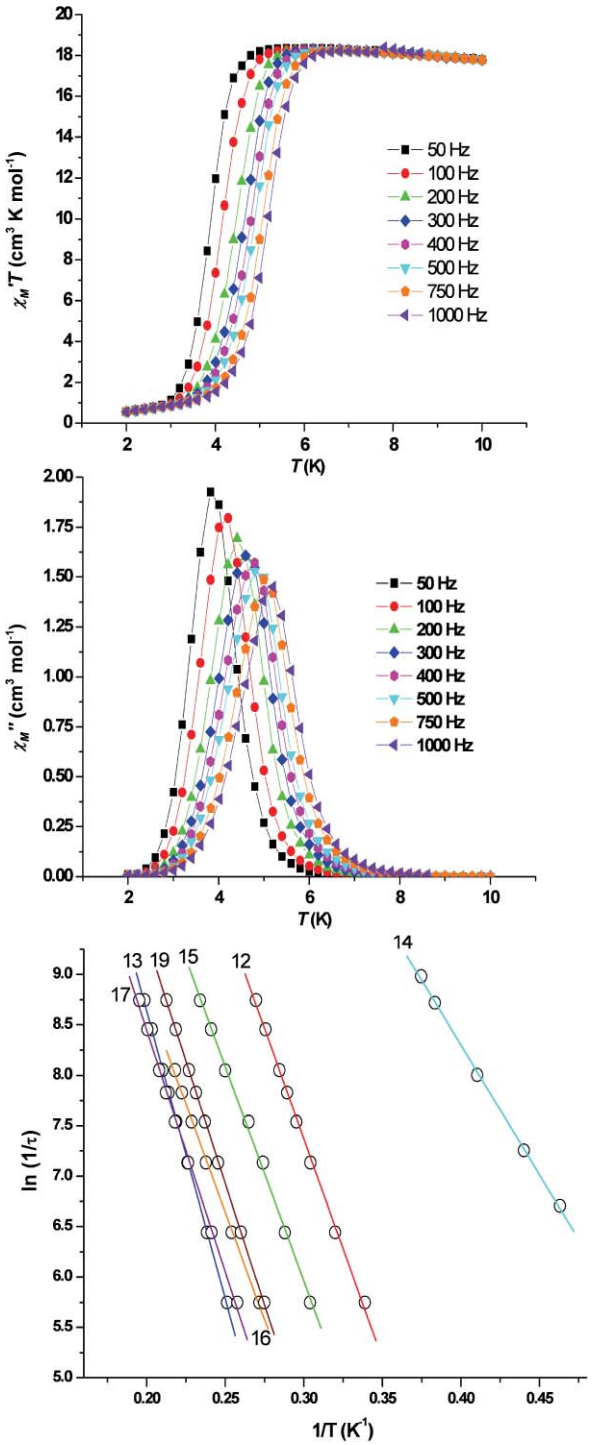

Fig. 6 Ac in-phase $\chi'_M T$ *vs.* T (top) and out-of-phase χ''_M *vs.* T (middle) plots obtained for complex **17** in an oscillating field of 3.5 Oe and frequencies of 50–1000 Hz. Plots of $\ln(1/\tau)$ *vs.* $1/T$ obtained from the ac magnetic susceptibility data for a cross section of family members (bottom).

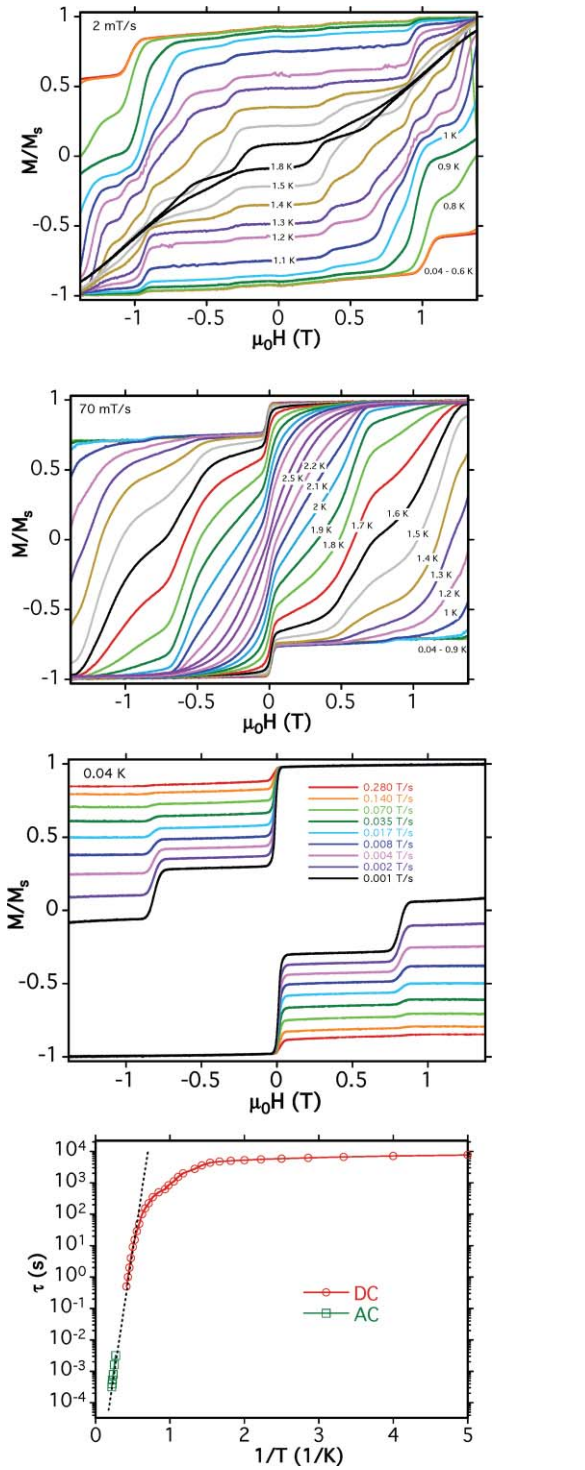

Fig. 7 Magnetisation *versus* field hysteresis loops for single crystals of **13** (top) and **16** (middle) at the indicated temperatures and field sweep rates. M is normalised to its saturation value. Arrhenius plot (bottom) using ac and dc data for **16**. The dashed line is the fit of the thermally activated region.

molecule are coupled antiferromagnetically to its neighbouring molecules, acting as a bias that shifts the quantum tunneling resonances with respect to the isolated SMM. The majority of the small steps observed in all the loops are therefore due to molecules having one (or several) "reversed" ("spin up - spin down") neighbouring molecules - though some may be attributed to multi-body quantum effects.[34] The complexity of the three dimensional H-bonding networks seen in the crystal structures makes it essentially impossible (or at least extremely difficult) to determine all of the active exchange paths and to identify all of the steps.

Type 3 molecules, however, in which the lower face of the [Mn_3] triangle is occupied by derivatized pyridine analogues show no significant H-bonding in the crystal and this is reflected in the appearance of much simpler looking hysteresis loops - particularly at the lowest temperatures measured (below 1.5 K). Those for **16** are shown in the middle and lower panels of Fig. 7. Above ~1.5 K the loops appear more complicated with the emergence of fine structure which can be attributed to the contribution of excited states, crystal defects, nuclear spins, dipolar interactions or most likely the disorder associated with one of the β-picoline ligands (see CIF file for full details†). Data obtained at very low temperatures however are remarkably simple showing only resonances originating from the ground state. The data obtained at 40 mK are shown in the lower-middle panel of Fig. 7 and show hysteresis loops with a step at zero field. A step indicates a surge in the magnetisation relaxation rate due to quantum tunnelling of the magnetisation through the barrier, occurring at a field position where there is an avoided level crossing. At $H = -1$ T all the molecules are in the $M_S = +6$ state. When the field is swept in a positive direction there is resonance between the +6 and −6 M_S levels at $H = 0$, and some of the molecules tunnel. As the field sweep rate is decreased a second step emerges at *ca.* 0.80 T. The separation between the steps is related to D by the equation $\Delta H = |D|/g\mu_B$. Measurement of the step positions for complex **16** thus afford an average field separation of ~0.8 T and thus a $|D|/g$ value of ~0.38 cm^{-1}. Assuming $g = 2.00$, this corresponds to a $|D|$ value of approximately 0.76 cm^{-1}, somewhat larger than that obtained from the dc magnetisation measurements (–0.52 cm^{-1}), and consistent with earlier comments regarding the validity of the D values obtained from the fit of the magnetisation *versus* field data, and with previous reports of analogous "uncoupled" [Mn^{III}_3] triangles; *i.e.* the magnitude of D for all four complexes appears to be somewhat underestimated. New clusters with these inter-molecular interactions (and disorder) removed will be required to get an accurate representation of the spin Hamiltonian parameters and of the relaxation dynamics. **16** represents a rare example of a rather simple SMM in which the influence of inter-molecular interactions and excited states are negligible at low temperatures. This is potentially an exciting discovery since it gives us access to a molecule containing only three metal ions that displays beautiful low temperature SMM behaviour and tunnel effects, and thus a model system with which to go beyond the giant spin approximation to potentially yield much fruitful physical information. Full details of the low temperature physics will be published in future papers.

High frequency electron paramagnetic resonance studies

High-frequency EPR measurements were performed at various discrete frequencies in the range from 52 to 344 GHz on single-crystals of complex **3** ($S = 2$), **12** ($S \approx 5$–6, *vide infra*) and **13** ($S = 6$) to verify their ground state spin values and zero field splitting (ZFS) parameters. Prior to measurement, crystals were quickly transferred from their mother liquor and coated in silicone grease in order to avoid solvent loss. The samples were also initially cooled under atmospheric helium gas, with a total transfer time from the mother liquor to the cryostat of ~5 minutes. An oversized cylindrical resonator was employed in order to provide enhanced sensitivity, and a Millimeter-wave Vector Network Analyzer (MVNA) served as a superheterodyne spectrometer. Both single- (complexes **3** and **13**) and double-axis (complexes **12** and **13**) field-orientation dependent studies were performed in order to insure magnetic field alignment either perpendicular or approximately parallel to the magnetic easy axes of the crystals. Details of the experimental technique can be found elsewhere.[35,36]

The most comprehensive study involved the high-symmetry (*R-3*) complex **13**, for which measurements were performed on separate crystals in two different spectrometers with single- (15 T) and double-axis (7 T) rotation capabilities. The quality of the hard-plane spectra obtained in the former were superior, but we first present high-frequency data obtained in the 7 T system. Angle-dependent studies were performed to obtain approximate alignment of the field with the sample's easy-axis. Once aligned, measurements were performed as a function of frequency and temperature so as to provide data sets which maximally constrain the axial ZFS parameters. Fig. 8 displays representative temperature dependent spectra obtained at 273 GHz (inset), together with plots of EPR peak positions deduced from measurements at four additional high frequencies (main panel, open symbols).

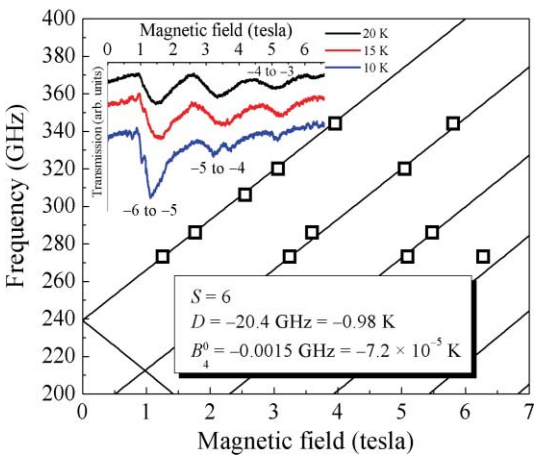

Fig. 8 Frequency dependence of EPR peak positions (black squares) obtained with the field applied approximately parallel to the easy-axis of **13**; the temperature was 20 K for these measurements. Superimposed on the data is the best simulation based on equation (5); the obtained ZFS parameters are given in figure. The inset displays representative spectra obtained at 273 GHz and at three different temperatures. The various fine structures have been labeled according to the spin projection along the easy axis.

Before discussing the simulations in Fig. 8 (solid lines in main panel), we comment on the spectra. The peaks are rather broad, indicating disorder in this crystals. It is also apparent that additional fine-structure splittings appear at the lowest temperature, which is a sign of intermolecular exchange interactions.[37] The data points in the main panel of Fig. 8 were extracted from the 20 K spectra so as to avoid complications due to such intermolecular interactions. The solid curves were simulated using the following spin Hamiltonian, containing only axial ZFS parameters.

$$\hat{H} = D\hat{S}_z^2 + B_4^0\,[35S_z^4 - \{30S(S+1)\}S_z^2] + \mu_B \mathbf{B}\cdot g\cdot\hat{S} \qquad (5)$$

The operators and fundamental constants in equation (5) are defined elsewhere,[37] and the obtained ZFS parameters are given in the figure. The most important observation is the robust agreement

with a spin $S = 6$ Hamiltonian. Attempts to fit to a spin state with $S < 6$ were unsuccessful. Thus, these EPR studies confirm the findings of the preceding magnetic studies. Nevertheless, evidence for considerable mixing between the ground and excited spin states is given by the significant 4th order ZFS parameter.[38] Interestingly, the values of D and B_4^0 are quite comparable to those reported recently for a family of very similar Mn_3 complexes.[28] In particular, there is a good correlation between B_4^0 and the exchange constant, J, among these complexes, *e.g.* $B_4^0 = -7.2 \times 10^{-5}$ K and $J = +4.0$ K for complex **13**, while B_4^0 ranges from -3.8×10^{-5} K to -11×10^{-5} K and J from +2.3 to 4.7 K for the FM complexes in ref. 28. This correlation is significant, because it provides further proof that the fourth order terms are a direct consequence of spin mixing between low-lying multiplets, *i.e.* J and B_4^0 are directly related.[38]

91 GHz temperature dependent spectra obtained for **13** with the field in the hard plane are displayed in Fig. 9. The spectra are superior to those presented in Fig. 8, likely due to a higher quality sample. The signal-to-noise is also vastly improved by virtue of the lower frequency employed. Nevertheless, the appearance of multiple peaks associated with each cluster of fine-structure transitions suggests the presence of multiple species in the crystal, very similar to recently reported results for a family of Ni_4 complexes.[39] These spectra and their temperature dependence are fully consistent with a spin $S = 6$ state possessing significant axial anisotropy. Indeed, simulations assuming $S = 6$ confirm the axial ZFS parameters obtained from the easy-axis measurements. However, the best simulation necessitates inclusion of transverse ZFS terms (see Fig. SI3†). The nature of these terms is not well determined, but this nevertheless suggests the presence of transverse anisotropy. Attempts to fit to an $S < 6$ model were unsuccessful.

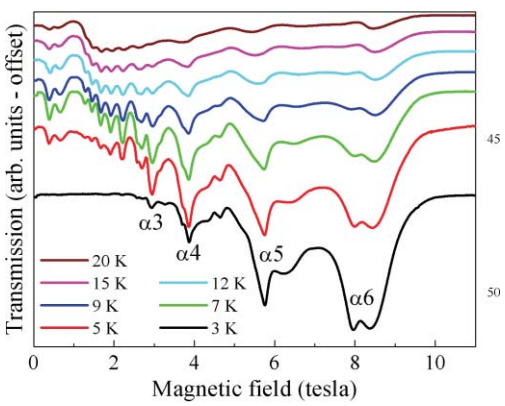

Fig. 9 Hard plane temperature dependence spectra obtained at 91 GHz for complex **13**; the fine structure peaks have been labeled according to a scheme described elsewhere.[40]

Plots of the 10 K EPR peak positions obtained from multi-frequency measurements on complex **12** with the field approximately aligned with its easy axis are displayed in Fig. 10. Simulations of these data are far less satisfactory than those for **13**. Indeed, simulations assuming $S = 5$ (Fig. 10(a)) are marginally better than those for $S = 6$ (Fig. 10(b)); the corresponding ZFS parameters are given in the figure. It is notable from Table 2 that complex **12** sits right at the borderline between the F and AF cases. It is thus very likely that the $S = 6$ state for **12** is not well developed, *i.e.* it is strongly mixed with low-lying $S < 6$ states. In this situation,

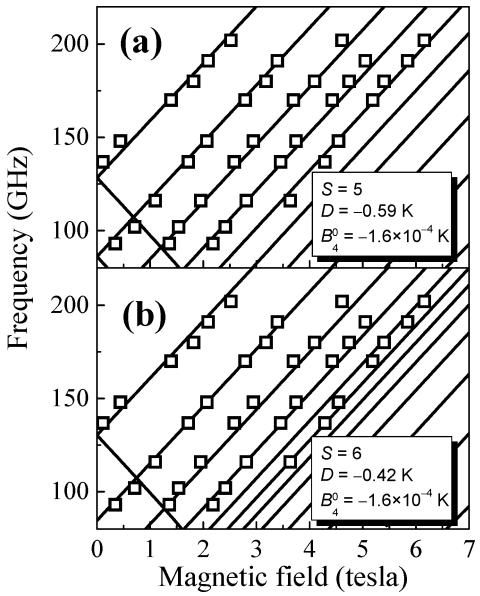

Fig. 10 Frequency dependence of EPR peak positions (black squares) obtained with the field applied approximately parallel to the easy-axis of **12**; the temperature was 10 K for these measurements. Superimposed on the data are simulations based on equation (5) with (a) $S = 5$ and (b) $S = 6$; the obtained ZFS parameters are given in the figure.

one would not expect good fits to equation (5), as confirmed in Fig. 10. Furthermore, the anisotropy is significantly depressed relative to complex **12**: the simulations in Fig. 10 suggest a barrier of only ~15 K (both for $S = 5$ and 6), in contrast to a value of 35 K for **13**. Note that both of these values are significantly lower than those deduced on the basis of magnetic studies (Table 2). This is not surprising given the marginal applicability of the models used to estimate these numbers (*e.g.* equation (4)). What is more, it has recently been shown that ac susceptibility measurements often overestimate the barrier, particularly for SMMs with low-lying excited spin multiplets.[41]

Finally, Fig. 11 shows hard-plane temperature dependent data obtained at 52 GHz for complex **3**. The overall appearance of the spectrum is consistent with that of a molecule with a relatively low spin quantum number (there are far fewer peaks as compared to Fig. 9) and a very significant axial anisotropy. However, it is not possible to make meaningful peak assignments or to fit data to

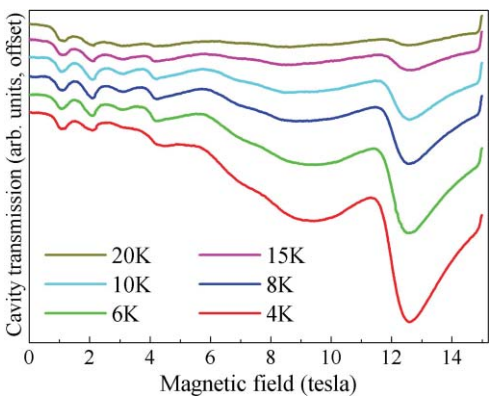

Fig. 11 Hard plane temperature dependence spectra of complex **3** obtained at 52 GHz.

equation (5). Nevertheless, one can make a crude estimate of the anisotropy on the basis of the position of the highest field (ground state) transition relative to the expected isotropic position (1.9 T for $g = 2$); this deviation ΔB provides a rough measure of the product of D and S or, rather, $|\frac{1}{2}D(2S-1)| \approx \Delta B \times 28$ GHz/T $\approx$ 336 GHz or 16 K.[37] If one assumes a spin $S = 2$ state, then this implies an extraordinarily large molecular D value of nearly −11 K (−7.5 cm^{-1}). From this, one can estimate an equally large single-ion D_1 value of approximately −5 cm^{-1} for the Mn^{III} ions (this assumes identical values for all three ions and parallel Jahn–Teller axes).[42] Note that a similar estimate for **13** gives a value for D_1 of approximately −2.6 cm^{-1}. While large, these values are not unprecedented.[43] Nevertheless, the value for **3** should not be taken too seriously given the many assumptions that went into estimating both the molecular and single-ion D values.

Discussion and conclusions

We have demonstrated three simple strategies for making ferromagnetic salicylaldoxime-based $[Mn^{III}_3]$ triangles, all of which are based on the deliberate puckering of the magnetic core of the molecule: a) when the parent oxime ligand ($saoH_2$) occupies the same plane as the $[Mn_3O]$ moiety, the Mn-N-O-Mn unit is easily made non-planar by derivatising the oximic carbon, *i.e.* by making R-$saoH_2$ ligands. When R = Et or Ph the puckering appears to be at its greatest. This effect is then re-inforced by (b) employing small "pincer" type tripodal ligands (ClO_4^-, ReO_4^- *etc*) to sit on the "upper" triangular face and (c) employing large sterically bulky ligands to occupy the "lower" triangular face. The combined effect is the production of highly distorted "bowl-shaped" molecules. When alcohol solvent molecules occupy the lower face, the molecules are involved in extensive H-bonding in the crystal lattice and the effect is clearly manifested in the magnetic behaviour and the triangles behave as exchange-biased SMMs. These inter-molecular interactions are removed and the molecules isolated from each other by replacing the alcohols with derivatized pyridine molecules such as β-picoline or ethyl-pyridine *etc*. The result is much "cleaner" and "simpler" magnetic data as reflected in both the bulk powder dc (and ac) data and the single-crystal hysteresis loop measurements. The emergence of families of such $[Mn_3]$ SMMs in which the influence of inter-molecular interactions and/or excited states can be nullified is an exciting discovery since it gives access to very simple molecules (3 spins) that display beautiful SMM behaviour and tunnelling effects, and model systems with which to go beyond the giant spin approximation to yield much fruitful physical information.[44]

Understanding the relationship between the structure and magnetic behaviour in these $[Mn_3]$ triangles, however, is a difficult task (even with twenty members) since one must consider all contributions to the exchange. This means we must consider the combination of different bridging and non-bridging ligand types (oxime, oxide, carboxylate or perchlorate, alcohol or pyridine); their relative positions and the bond lengths and angles associated with each. In earlier work on analogous $[Mn_6]$ complexes we discovered that the *dominant* factor governing the exchange between nearest neighbours appeared to be the twisting of the Mn-O-N-Mn moiety with respect to the $[Mn_3]$ plane as induced by the distortion imposed on the molecule by bulkier oximes (R-sao^{2-}). An examination of the data of Tables 1 and 2 suggests that this also appears to be true here, with the more puckered triangles displaying larger (more positive) exchange constants and the more planar triangles displaying more negative exchange constants. There does not appear to be any obvious correlation between J and the out-of-plane shift of the central oxide, the Mn-(μ_3-O)-Mn angle, the Mn^{III}-O^{2-} distances, or the Mn-N-O-Mn distances. For example, the presence of the carboxylate *versus* perchlorate/perrhenate seems to have little influence and there are antiferromagnetic triangles in which the central oxide is displaced more from the $[Mn_3]$ plane than that seen in the ferromagnetic triangles. For the $[Mn_6]$ family a Mn-N-O-Mn torsion angle of around 31° proved to be the "switching point", consistent with that observed here. Of course this analysis is purely *qualitative* in nature, since in each case we simulated the experimental susceptibility data using the most simple model possible. Indeed even with 21 members to dissect, definitive answers are difficult to come by. It is clear that the majority of family members are rather complicated molecules and we will need to synthesise and analyse more of the "isolated" siblings to gain more understanding.

Experimental procedures

All manipulations were performed under aerobic conditions, using materials as received. **CAUTION!** Although no problems were encountered in this work, care should be taken when using the potentially explosive perchlorate anion.

The syntheses, structures and magnetic properties of complexes **1**, **3**, **5-6**, **8-9**, **12-13**, **15**, **19** and **20** have already been communicated or reported. Compounds **2**, **4**, **7**, **10-11**, **14**, **16-18** and **21** are reported here for the first time.

General synthetic strategies:

For complexes **2**, **16-18** and **21**: $Mn^{II}(ClO_4)_2{\cdot}6H_2O$ (1 mmol) and the (derivatized) salicyaldoxime ligand R-$saoH_2$ (R = H, naphth, Et, Ph) (1 mmol) were dissolved in a mixture of pyridine (or derivatized pyridine) (5 ml) and MeOH (20 ml) with NEt_4OH (1 mmol). For **21**, $NaReO_4$ (1 mmol) was also added to the reaction mixture. The solutions were left stirring for ~1 h and then filtered. Et_2O was diffused into one half of the solution and the remainder was left to slowly evaporate. Suitable crystals grew after 3–5 days from both solutions.

For complex **4**: A pyridine/EtOH solution (25 ml) of $Mn^{II}(O_2CC_{10}H_7)^2{\cdot}H_2O$ (1 mmol), $saoH_2$ (1 mmol) and NEt_4OH (1 mmol) was stirred for ~1 h. After filtering single crystals grew upon slow evaporation during 5 days.

For complex **7**: $Mn^{II}(O_2CCH_3)_2{\cdot}4H_2O$ (1 mmol), Me-$saoH_2$ (1 mmol) and NMe_4ClO_4 (1 mmol) were dissolved in MeOH (25 ml) and NEt_4OH (1 mmol) added. After stirring for ~1 h the solution was filtered and allowed to evaporate. Crystals suitable for X-ray diffraction grew after 5 days.

For complex **10**: $Mn^{II}(ClO_4)_2{\cdot}6H_2O$ (1 mmol), ^{t}Bu-$saoH_2$ (1 mmol) and $HO_2CPh(OMe)_3$ were dissolved in a mixture of pyridine (5 ml) and EtOH (20 ml). NEt_4OH (1 mmol) was added and the mixture stirred for 2 hours before being filtered and allowed to slowly evaporate. Crystals suitable for X-ray diffraction grew after 5 days.

For complex **11**: $Mn^{II}(ClO_4)_2{\cdot}6H_2O$ (1 mmol), ^{t}Bu-$saoH_2$ (1 mmol) and $NaO_2CPh(CH_3)_2$ were dissolved in MeOH (20 ml). CH_3ONa (1 mmol) was added and the mixture stirred for 2 hours

before being filtered and allowed to slowly evaporate. Crystals suitable for X-ray diffraction grew after 5 days.

For complex **14**: $Mn^{II}(O_2CPh)_2{\cdot}2H_2O$ (1 mmol), Et-saoH_2 (1 mmol) and teaH_3 (1 mmol) were dissolved in EtOH (25 ml). After stirring for 1̃ h the solution was filtered and allowed to slowly evaporate. Crystals suitable for X-ray diffraction grew after 5 days.

Elemental Anal. calcd (found) for dried **2** solvent free: C 50.09 (50.37), H 4.20 (4.08), N 8.34 (8.15). **4**: C 58.17 (57.70), H 3.94 (3.93), N 9.13 (9.01). **7**: C 46.90 (46.73), H 5.35 (4.71), N 5.61 (5.48). **10**: C 58.48 (58.41), H 5.48 (4.88), N 7.33 (6.99). **11**(-3MeOH): C 55.20 (55.75), H 5.60 (5.19), N 4.49 (4.73). **14**: C 49.84 (49.31), H 5.72 (5.46), N 4.74 (4.56). **16**: C 51.52 (51.62), H 4.61 (4.49), N 8.01 (8.09). **17**: C 52.76 (52.94), H 5.40 (5.28), N 7.38 (7.60). **18**: C 55.18 (55.41), H 5.66 (5.68), N 7.15 (6.92). **21**: C 57.73 (57.75), H 4.05 (3.25), N 7.04 (6.48).

Variable temperature, solid-state direct current (dc) and alternating current (ac) magnetic susceptibility data down to 1.8 K were collected on a Quantum Design MPMS-XL SQUID magnetometer equipped with a 7 T dc magnet. Diamagnetic corrections were applied to the observed paramagnetic susceptibilities using Pascal's constants. Magnetic studies below 1.8 K were carried out on single crystals using a micro-SQUID apparatus operating down to 40 mK.

Diffraction data were collected at 150 K on a Bruker Smart Apex CCDC diffractometer, equipped with an Oxford Cryosystems LT device, using Mo radiation. See CIF files† for full details.[45]

Notes and references

1 D. Gatteschi and R. Sessoli, *Angew. Chem., Int. Ed.*, 2003, **42**, 268.
2 R. Sessoli, D. Gatteschi, A. Caneschi and M. A. Novak, *Nature*, 1993, **365**, 141.
3 W. Wernsdorfer and R. Sessoli, *Science*, 1999, **284**, 133.
4 W. Wernsdorfer, N. Aliaga-Alcalde, D. N. Hendrickson and G. Christou, *Nature*, 2002, **416**, 406.
5 S. Hill, R. S. Edwards, N. Aliaga-Alcalde and G. Christou, *Science*, 2003, **302**, 1015.
6 M. N. Leuenberger and D. Loss, *Nature*, 2001, **410**, 789.
7 A. Caneschi, D. Gatteschi, N. Lalioti, C. Sangregorio, R. Sessoli, G. Venturi, A. Vindigni, A. Rettori, M. G. Pini and M. A. Novak, *Angew. Chem., Int. Ed.*, 2001, **40**, 1760.
8 S. Carretta, P. Santini, G. Amoretti, M. Affronte, A. Candini, A. Ghirri, I. S. Tidmarsh, R. H. Laye, R. Shaw and E. J. L. McInnes, *Phys. Rev. Lett.*, 2006, **97**, 207201.
9 F. Troiani, A. Ghirri, M. Affronte, S. Carretta, P. Santini, G. Amoretti, S. Piligkos, G. Timco and R. E. P. Winpenny, *Phys. Rev. Lett.*, 2005, **94**, 207208.
10 J. Lehmann, A. Gaita-Arino, E. Coronado and D. Loss, *Nat. Nanotechnol.*, 2007, **2**, 312.
11 E. Coronado, J. R. Galán-Mascarós, C. J. Gómez-García and V. Laukhin, *Nature*, 2000, **408**, 447.
12 M. Evangelisti, A. Candini, A. Ghirri, M. Affronte, E. K. Brechin and E. J. L. McInnes, *Appl. Phys. Lett.*, 2005, **87**, 072504.
13 L. Bogani and W. Wernsdorfer, *Nat. Mater.*, 2008, **7**, 179.
14 D. Gatteschi, R. Sessoli and J. Villain, *Molecular Nanomagnets*, Oxford University Press, Oxford, 2006.
15 G. Aromí and E. K. Brechin, *Struct. Bonding*, 2006, **122**, 1, and references therein.
16 R. Bircher, G. Chaboussant, C. Dobe, H. U. Güdel, S. T. Ochsenbein, A. Sieber and O. Waldmann, *Adv. Funct. Mater.*, 2006, **16**, 209.
17 M. Evangelisti, F. Luis, L. J. de Jongh and M. Affronte, *J. Mater. Chem.*, 2006, **16**, 2534.
18 M. Affronte, S. Carretta, G. A. Timco and R. E. P. Winpenny, *Chem. Commun.*, 2007, 1789.
19 G. A. Timco, S. Carretta, F. Troiani, F. Tuna, R. J. Pritchard, C. A. Muryn, E. J. L. McInnes, A. Ghirri, A. Candini, P. Santini, G. Amoretti, M. Affronte and R. E. P. Winpenny, *Nat. Nanotechnol.*, 2009, **4**, 173.
20 C.-F. Lee, D. A. Leigh, R. G. Pritchard, D. Schultz, S. J. Teat, G.A Timco and R. E. P. Winpenny, *Nature*, 2009, **458**, 314.
21 G. Christou, *Polyhedron*, 2005, **24**, 2065.
22 S. G. Sreerama and S. Pal, *Inorg. Chem.*, 2002, **41**, 4843.
23 T. C. Stamatatos, D. Foguet-Albiol, C. C. Stoumpos, C. P. Raptopoulou, A. Terzis, W. Wernsdorfer, S. P. Perlepes and G. Christou, *J. Am. Chem. Soc.*, 2005, **127**, 15380.
24 (*a*) C. J. Milios, PhD Thesis, University of Patras, Greece, 2004; (*b*) C. J. Milios, A. G. Whittaker and E. K. Brechin, *Polyhedron*, 2007, **26**, 1927.
25 R. D. Cannon and R. P. White, *Prog. Inorg. Chem.*, 1988, **36**, 195.
26 (*a*) R. Inglis, L. F. Jones, C. J. Milios, S. Datta, A. Collins, S. Parsons, W. Wernsdorfer, S. Hill, S. P. Perlepes, S. Piligkos and E. K. Brechin, *Dalton Trans.*, 2009, 3403; (*b*) C. J. Milios, S. Piligkos and E. K. Brechin, *Dalton Trans.*, 2008, 1809; (*c*) C. J. Milios, R. Inglis, A. Vinslava, R. Bagai, W. Wernsdorfer, S. Parsons, S. P. Perlepes, G. Christou and E. K. Brechin, *J. Am. Chem. Soc.*, 2007, **129**, 12505; (*d*) C. J. Milios, R. Inglis, R. Bagai, W. Wernsdorfer, A. Collins, S. Moggach, S. Parsons, S. P. Perlepes, G. Christou and E. K. Brechin, *Chem. Commun.*, 2007, 3476; (*e*) C. J. Milios, A. Vinslava, W. Wernsdorfer, A. Prescimone, P. A. Wood, S. Parsons, S. P. Perlepes, G. Christou and E. K. Brechin, *J. Am. Chem. Soc.*, 2007, **129**, 6547; (*f*) C. J. Milios, A. Vinslava, S. Moggach, S. Parsons, W. Wernsdorfer, G. Christou, S. P. Perlepes and E. K. Brechin, *J. Am. Chem. Soc.*, 2007, **129**, 2754; (*g*) C. J. Milios, A. Vinslava, P. A. Wood, S. Parsons, W. Wernsdorfer, G. Christou, S. P. Perlepes and E. K. Brechin, *J. Am. Chem. Soc.*, 2007, **129**, 8.
27 (*a*) R. Inglis, L. F. Jones, G. Karotsis, A. Collins, S. Parsons, S. P. Perlepes, W. Wernsdorfer and E. K. Brechin, *Chem. Commun.*, 2008, 5924; (*b*) R. Inglis, L. F. Jones, K. Mason, S. P. Perlepes, W. Wernsdorfer and E. K. Brechin, *Chem.–Eur. J.*, 2008, **14**, 9117; (*c*) C. J. Milios, R. Inglis, L. F. Jones, A. Prescimone, S. Parsons, W. Wernsdorfer and E. K. Brechin, *Dalton Trans.*, 2009, 2812.
28 P. L. Feng, C. Koo, J. J. Henderson, P. Manning, M. Nakano, E. del Barco, S. Hill and D. N. Hendrickson, *Inorg. Chem.*, 2009, **48**, 3480.
29 (*a*) M. O'Keeffe, M. A. Peskov, S. J. Ramsden and O. M. Yaghi, *Acc. Chem. Res.*, 2008, **41**, 1782; (*b*) V. A. Blatov, *IUCr CompComm Newsletter*, 2006, **7**, 4 http://www.topos.ssu.samara.ru.
30 J. J. Borras-Alemnar, J. M. Clemente-Juan, E. Coronado and B. S. Tsukerblat, *J. Comp. Chem.*, 2001, **22**, 985.
31 S. Piligkos, *MAGMOFIT*, The University of Copenhagen.
32 (*a*) W. Wernsdorfer, *Adv. Chem. Phys.*, 2001, **118**, 99; (*b*) W. Wernsdorfer, *Supercond. Sci. Technol.*, 2009, **22**, 064013.
33 R. Tiron, W. Wernsdorfer, N. Aliaga-Alcalde and G. Christou, *Phys. Rev. B: Condens. Matter Mater. Phys.*, 2003, **68**, 140407.
34 (*a*) W. Wernsdorfer, S. Bhaduri, R. Tiron, D. N. Hendrickson and G. Christou, *Phys. Rev. Lett.*, 2002, **89**, 197201; (*b*) W. Wernsdorfer, S. Bhaduri, A. Vinslava and G. Christou, *Phys. Rev. B: Condens. Matter Mater. Phys.*, 2005, **72**, 214429.
35 M. Mola, S. Hill, P. Goy and M. Gross, *Rev. Sci. Instrum.*, 2000, **71**, 186.
36 S. Takahashi and S. Hill, *Rev. Sci. Instrum.*, 2005, **76**, 023114.
37 E. del Barco, A. D. Kent, S. Hill, J. M. North, N. S. Dalal, E. M. Rumberger, D. N. Hendrickson, N. Chakov and G. Christou, *J. Low Temp. Phys.*, 2005, **140**, 119.
38 A. Wilson, J. Lawrence, E-C. Yang, M. Nakano, D. N. Hendrickson and S. Hill, *Phys. Rev. B: Condens. Matter Mater. Phys.*, 2006, **74**, 140403.
39 J. Lawrence, E.-C. Yang, R. Edwards, M. M. Olmstead, C. Ramsey, N. S. Dalal, P. K. Gantzel, S. Hill and D. N. Hendrickson, *Inorg. Chem.*, 2008, **47**, 1965.
40 S. Takahashi, R. S. Edwards, J. M. North, S. Hill and N. S. Dalal, *Phys. Rev. B: Condens. Matter Mater. Phys.*, 2004, **70**, 094429.
41 C. Lampropoulos, S. Hill and G. Christou, *ChemPhysChem*, 2009, **10**, 2397–2400.
42 S. Datta, E. Bolin, C. J. Milios, E. K. Brechin and S. Hill, *Polyhedron*, 2009, **28**, 1788.
43 J. Krzystek, A. Ozarowski and J. Telser, *Coord. Chem. Rev.*, 2006, **250**, 2308.
44 Detailed studies of the single crystal measurements will appear in future papers.
45 D. J. Watkin, C. K. Prout, J. R. Carruthers, P. W. Betteridge and R. I. Cooper, *CRYSTALS*, Issue 12, 2003, Chemical Crystallography Laboratory, University of Oxford, Oxford, UK.

